



# Detection of Ore Type in Drilling Cores Using Machine Vision Algorithm

Pouya Nobahar<sup>1\*</sup>, Yashar Pourrahimian<sup>2</sup>, Roohollah Shirani Faradonbeh<sup>3</sup>, and Fereydoun Mollaei Koshki<sup>4</sup>

1. ARC Training Centre for Integrated Operations for Complex Resources, The University of Adelaide, Adelaide, Australia

2. School of Mining and Petroleum Engineering, University of Alberta, Canada

3. WA School of Mines: Minerals, Energy and Chemical Engineering, Curtin University, Australia

4. Iran China Clay Industry Co., Iran

## Article Info

Received 17 May 2024

Received in Revised form 30 July 2024

Accepted 30 August 2024

Published online 30 August 2024

DOI: [10.22044/jme.2024.14538.2739](https://doi.org/10.22044/jme.2024.14538.2739)

## Keywords

Artificial Intelligence

Image processing

Classification

Optimization

Borehole

## Abstract

Mineral reserve evaluation and ore type detection using data from exploratory boreholes are critical in mine design and extraction. However, preparing core samples and conducting chemical and physical tests is a time-consuming and costly procedure, slowing down the modeling process. This paper presents a novel Deep Learning (DL)-based model to recognize the types of kaolinite samples. For this purpose, a dataset containing the images of drilled cores and their types determined from conventional chemical and physical analyses was used. Eight Convolutional Neural Network (CNN) topologies based on individual features were developed, named A, B, C, D, E, F, G, and H. Six of the eight proposed CNN topologies described above had accuracy below 80%, whereas two of them, model A and H, had higher accuracy than other topologies. Due to their similarity in results, both of them analyzed deeply. Model A was more efficient, with 90% accuracy, than model B, with 84% accuracy. Furthermore, the class detection performance of model A was further evaluated using different indices, including precision, recall, and F1-score, which resulted in values of 92%, 92%, and 90%, respectively, which are acceptable accuracies to identify the type of samples when using this approach on six different types of kaolinite.

## 1. Introduction

The use of exploratory borehole data in mine design and evaluation of mineral reserves is one of the essential stages of mining operations, significantly affecting the project's viability. In conventional approaches, chemical and physical tests are performed on drilled cores to quantify the sample elements. These analyses are either employed on a continuous basis (grades) or as classifications. Preparing core samples and conducting chemical and physical tests is time-consuming and costly, slowing down the modeling process [1–3]. However, standard methodologies have been upgraded by combining industrial and computer science to obtain a realistic approach. For

instance, in the study conducted by Lepisto et al. [4], the texture characteristics were derived from real rock photos in which, using various scales, they applied a Gaussian bandpass filter to the image's color channels in RGB (red, green, blue) and HIS (hue, saturation, intensity) color spaces. The results showed that combining different color channels improves categorization accuracy substantially. In another study, Singh and Rao [5] proposed a new method for classifying ores in ferromanganese metallurgical plants. Their approach is based on the visual texture of the manganese-enriched particles (steel gray colored), iron-enriched particles (reddish brown), alumina-

✉ Corresponding author: [a1900269@adelaide.edu.au](mailto:a1900269@adelaide.edu.au) (P. Nobahar)

enriched particles, and Radial Basis Neural Network (RBNN). The results demonstrated that the technique might be used to construct an expert system for online ore quality monitoring, which can be used to manage ore blending in feed ore circuits and separate gangue minerals in feed ores. In 2010, Baykan and Yilmaz [6] used color spaces and Artificial Neural Networks (ANNs) to investigate mineral identification. Their proposed network classifies five different minerals (quartz, muscovite, biotite, chlorite, and opaque) using six input parameters (i.e., Red, Green, and Blue colors and images' hue, saturation, and value). The network resulted in an accuracy value ranging from 81% to 98%, representing the high detection performance of the model. Chatterjee et al. [4] used a neural network model as a mapping function for ore quality monitoring and grade prediction in 2010. The findings showed that this approach might be utilized to monitor ore grade at the mine level in a controlled setting. By using image processing and pattern recognition approaches, Khorram et al. [7] created an ore-grade prediction model in 2012. The concept accurately predicted the proportion of chemical constituents of samples taken from the same mine. In 2013, Keyvani and Strom [8] created a fully-automated image processing script for analyzing massive datasets of photographed flocs in mud suspensions in dilute turbulent suspensions. Liu et al. [9] developed a software called "Crack Image Analysis System" (CIAS) to evaluate the geometric features of crack networks in 2013. Various geometric characteristics, such as node number, crack number, clod area, clod perimeter, crack area, width, length, and direction, can be determined automatically using this program. In addition, Gan and Scholz [10] proposed a technique in 2013 for measuring and precisely extracting lamina characteristics from sedimentary core pictures. In 2016, Patel and Chatterjee [11] proposed a computer vision-based rock-type classification system for quick and accurate detection without human interference. In their study, a Probabilistic Neural Network (PNN) with color histogram data as feed was utilized to construct a laboratory-scale vision-based model. The cumulative miss-

classification loss for this approach was less than 6%.

Chauhan et al. [12] looked at how to segment X-ray digital microtomography rock pictures and predict pore spacing and pore size using unsupervised, supervised, and ensemble clustering algorithms. Abhik et al. [13] developed a mass framework in 2016 that translates the image-based size distribution to a mass-wise distribution, enabling its comparison with mechanical filtration data. In their paper, for mass rebuilding from 2D pictures of particle aggregates, the idea of weight/particle ratio was presented. In 2018, Ramil et al. [14] proposed a backpropagation ANN-based model to recognize granite formation minerals quickly and precisely using RGB images. Their research led to identifying the constituent minerals for three different granitic rock types with high accuracy. In 2019, Maitre et al. [15] proposed a novel methodology for automating mineral grains recognition from numerical images obtained with a simple optical microscope. Their method generates super-pixels using basic linear iterative grouping segmentation, and almost all of them permit separating sand grains, which is impossible with traditional segmentation approaches. In 2019, Ran et al. [16] reported an efficient measure for recognizing rock types in the field using a Convolutional Neural Network (CNN) algorithm and image analysis technique. With excellent prediction performance, the suggested method was successfully used to identify six common rock types. In another study in 2019, Ouanan and El Hassan [17] suggested a real-time froth image processing method in the field of mineral processing. The main objective of their study was to investigate the numerous possibilities of cutting-edge image processing (IP) and machine learning (ML) techniques for mapping and mineral processing. Additionally, a real-time machine vision application for froth image analysis in the context of mineral processing has been developed. Finally, they suggested several future directions, such as data analysis and building an exploration tool based on IP and ML algorithms by analyzing geoscience datasets using cloud computing technology to discover target locations with significant development.

Safari et al. [18] published an IP approach for analyzing pore and grain size variations in porous geological rocks using X-ray microcomputed tomography and scanning electron microscopy (SEM) images in 2021. Furthermore, Liu et al. [19] created four CNN-based models having different depths and topologies for multi-coal and multi-class image analysis in 2021. Additionally, they examined the factors that influenced classification weight and exposed the operational procedures of CNN's model in coal image recognition and classification using the Channel Visualization map, Heatmap, Grad-CAM map, and Guided Backpropagation map. Fathi et al. [20] employed optimization clustering and neural network algorithms to estimate the iron grade in the Choghart iron ore located in Iran. The results from both the training and testing phases highlight the optimized neural network system's significant proficiency in ore grade estimation. An approach was developed to integrate IP/RS geophysical attributes with borehole grade analyses and geological data using the cuckoo search machine learning algorithm to estimate silver grade values by Alimoradi et al [21]. The findings demonstrate that grade values can be accurately estimated from geophysical data, particularly in regions lacking drilling data. The potential of ensemble learning models for lithological classification was thoroughly examined by Farhadi et al. [22], implementing boosting, stacking, and bagging models proved superior to traditional methods such as LR and SVM. Furthermore, another study by Farhadi et al. [23] aimed to utilize ML model predictions to classify Pb and Zn anomalies through concentration-area fractal modeling in the study area. The fractal model results identified five geochemical populations for both elements. The primary anomalous regions of these elements were associated with mining activities and core drilling data, indicating that our method holds promise for predicting ore elemental distribution. A study by Afzal et al. [24] shows that the hybrid model has substantial potential for predicting ore elemental distribution. The model presented promising results and can accurately predict ore grades in similar investigations.

According to the above literature review, advanced AI-based techniques have been extensively used by researchers and mining engineers over the past few years due to their capabilities in solving high-complex problems. However, most prior studies and proposed models are based on a limited database. On the other hand, the prior studies required some laboratory devices and could not identify rock types accurately in a short time. Also, none of them can classify subclasses of a unique mineral. In this study, deep learning (DL) algorithm and images related to kaolinite types are used, and eight different CNNs are executed. Then, a model with a fast execution speed, low cost, and high accuracy is presented to classify the various types of kaolinite samples instead of traditional methods like chemical and physical analyses.

## 2. Deep Learning and Convolutional Neural Network

The ability of ML algorithms to learn from data and make predictions or decisions without being explicitly programmed has increased their popularity across various academic fields. One of the most advanced techniques in this field has been used in this study to estimate the type of minerals from various input photos. As shown in Figure 1, DL is a subfield of ML that enables computers to learn from past experiences and comprehend their surroundings via layered structures. DL is built on adaptive, durable, and scalable ANNs, making it ideal for large and complex ML challenges like image categorization [25].

On the other hand, CNN is a subset of ANN designed to deal with data with a known, grid-like structure, such as image data. Fu and Aldrich [26] have comprehensively reviewed DL in mining and mineral processing operations. Their research revealed that CNNs compared to other DL algorithms (i.e., long short-term memory recurrent networks LSTMs, deep belief networks DBNs, and deep reinforcement learning DRL), have been extensively used in solving mining-related problems (see Figure 2). CNN uses a mathematical method known as convolution, a form of linear operation, to create its network [25]. Tensor-Flow, an end-to-end open-source ML framework, can be

used to implement CNN. Also, Keras is a Python-based high-level neural network API used with Tensor-Flow. In this study, these platforms were used to create and execute models and networks.

Recursive neural networks (RvNNs), recurrent neural networks (RNNs), and convolutional neural

networks (CNNs) are the most well-known varieties of DL networks. RvNN can categorize data and predict output in a hierarchical framework using compositional vectors [27].

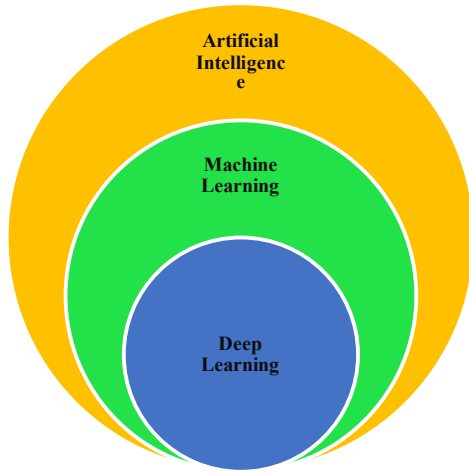


Figure 1. Artificial Intelligence and its subsets

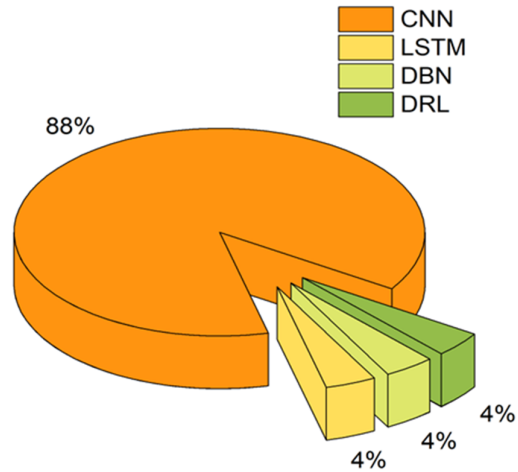


Figure 2. Application of DL algorithms in mining [19]

### 2.1. DL and CNN applications

CNN is the most well-known and widely used method in DL. The fundamental characteristic of CNN over its predecessors is that it automatically detects significant elements without the need for human intervention [28]. Nearly all scientific domains have been impacted by this technology, as seen in Figure 3.

The use of DL has already disrupted and revolutionized the majority of sectors and businesses. The world's top IT and business-oriented companies are competing to advance DL. CNNs have been widely used in a variety of domains, including computer vision [29], voice recognition [30], and face recognition [31]. On the other hand, this technology has been employed in various engineering fields to enhance the proficiency of operations [32-37], for example, assisting the healthcare section in diagnosing illness and find drugs [38-45], improving agricultural operations by detecting plant diseases [46, 47], identifying land cover [48], and counting fruits [49]. Furthermore, it helps urban experts find better ways to increase the life quality of citizens [50-53].

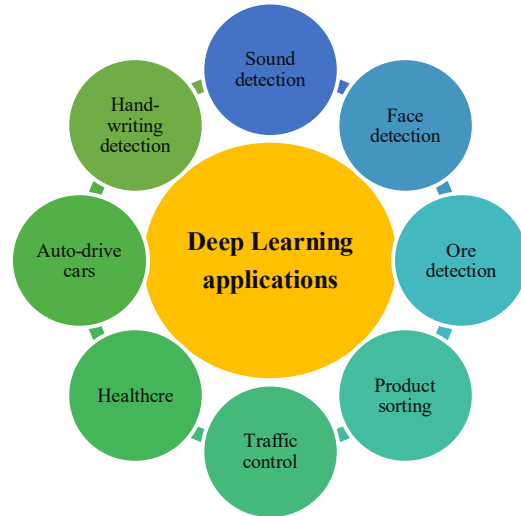


Figure 3. Applications of Deep Learning

The benefits of using CNNs over other traditional neural networks in the computer vision environment are (i) the weight sharing feature, which reduces the number of trainable network parameters and, in turn, helps the network to enhance generalization and avoid overfitting, (ii) concurrently learning the feature extraction layers and the classification layer causes the model output to be both highly organized and highly reliant on

the extracted features, and (iii) large-scale network implementation, which is much easier with CNN than with other neural networks [21].

### 2.2. CNN architecture

Figure 4 shows an illustration of a CNN architecture for image categorization. CNNs have

several distinct layers. The convolutional layer, pooling layer, activation function, fully connected layer, and loss function are the main components of a CNN model, which are discussed in the following sections.

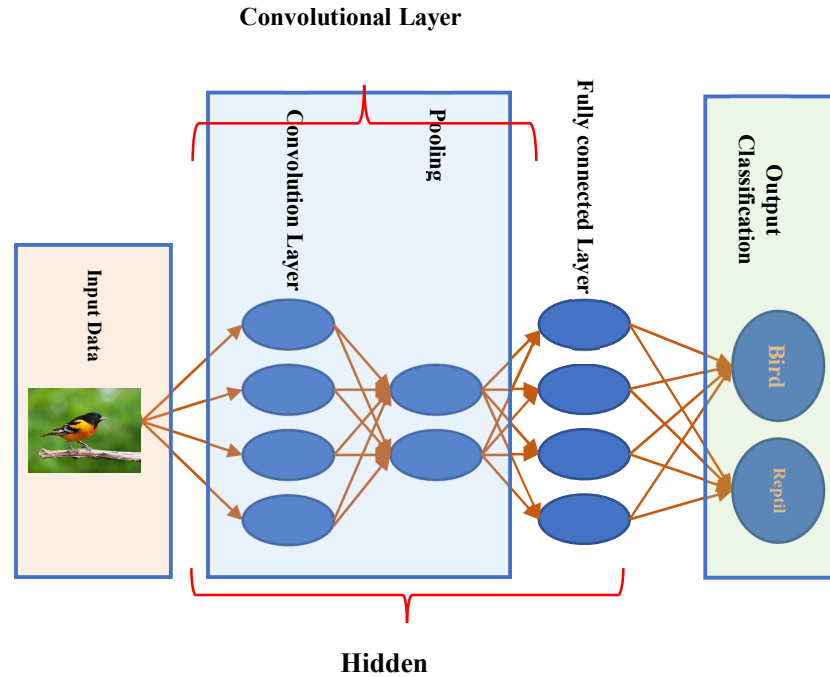


Figure 4. A CNN layers' architecture

#### 2.2.1. Convolutional layer

The convolutional layer is the most important part of the CNN architecture. It is made up of a number of convolutional filters called kernels. The input image, expressed as N-dimensional metrics, is convolved with these filters to generate the output feature map [54]. As feature extractors, convolutional layers learn the features of the input images by passing a filter over them and creating a feature map. Then, nonlinearity is applied to the result. The  $k$ th output feature map is computed as follows:

$$Y_k = f(w_k * x) \tag{1}$$

where  $x$  is the input picture,  $w_k$  is the convolutional filter associated with the  $k$ th feature

map,  $f$  is the nonlinear activation function, and [55], and  $Y_k$  is the  $k$ th input of the next layer [56].

#### 2.2.2. Pooling layer

The feature maps' subsampling is the pooling layer's main function. Convolutional operations are used to create these maps. In other words, this method leads to the creation of reduced-size large-scale feature maps. At the same time, it keeps most of the dominant data (or characteristics) during the entire pooling stage. Several pooling strategies can be used at different pooling levels. These techniques include Global Average Pooling (GAP), global max pooling, gated pooling, and average pooling. The max, average, and GAP pooling techniques shown in Figure 5 are the most well-known and widely used pooling techniques [57, 58].

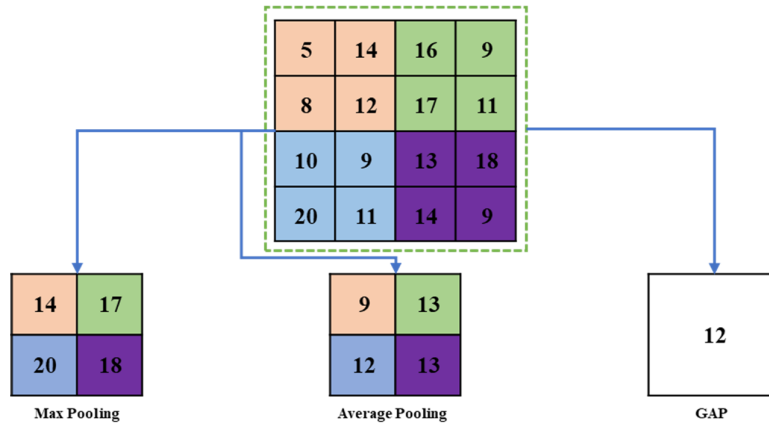


Figure 5. Example of minimum, average, and global average pooling methods

2.2.3. Activation function

Activation functions help CNNs show complex characteristics. The model's activation function is like a control center that decides what information to send to the next neuron and works like the human brain neurons. In a neural network, every neuron takes the result from the neurons in the earlier layers and sends it to the next layer after processing it [59]. Figure 7 illustrates the activation function's structure. In Figure 6,  $x_i$  represents the

input feature;  $n$  features are input to the neuron  $j$  at the same time;  $x_{ij}$  represents the weight value of the connection between the input feature  $x_i$  and the neuron  $j$ ;  $b_j$  represents the internal state of the neuron  $j$ , which is the bias value; and  $y_j$  is the output of the neuron  $j$ .  $f(0)$  is the activation function, which can be the sigmoid function (Equation 2), tanh function (Equation 3) [60], rectified linear unit ((ReLU) Equation4) [61], and softmax (Equation5) [62].

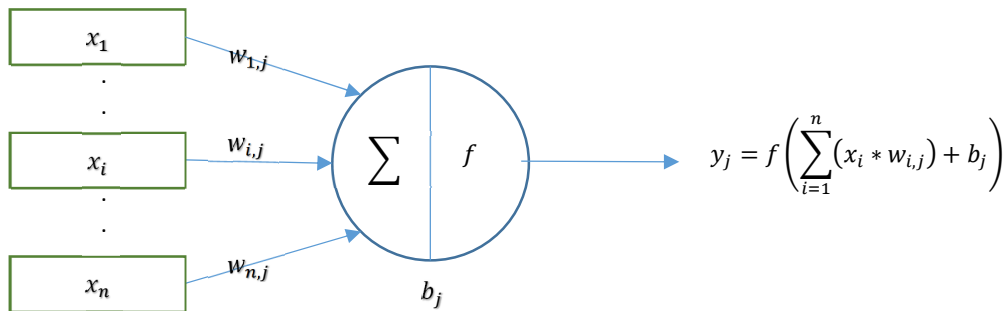


Figure 6. General activation function structure [59]

$$Sigmoid(x) = \frac{1}{1 + e^{-x}} \tag{2}$$

$$TanH(x) = \frac{2}{1 + e^{-2x}} - 1 \tag{3}$$

$$ReLU(x)/Rectified\ Linear\ Unit(x) = Max(x, 0) \tag{4}$$

$$Softmax = \sigma(x_j) = \frac{e^x}{\sum_i e^{x_i}} \tag{5}$$

The fundamental purpose of all activation functions in every kind of neural network is to map the input to the output. The weighted summation of the neuron input and its bias (if present) is computed to get the input value. This means that by producing the corresponding output, the activation function decides whether or not to fire a neuron in response to a specific input. Another crucial requirement for the activation function is differentiation, which enables error backpropagation to be utilized for training the

network. In CNNs and other deep neural networks, the Sigmoid, Tanh, and ReLU functions are most frequently utilized activators [54].

#### 2.2.4. Fully connected layer

This layer is usually at the end of each CNN design. The Fully Connected (FC) technique connects each neuron in a layer to all the neurons in the previous layer. It works like a regular neural network that moves information forward. The FC layer gets information from the prior layer, which could either be a pooling or convolutional layer. This vector is made from the feature maps when they have been [63, 64].

#### 2.2.5. Loss functions

The last part of the CNN structure is called the output layer. It is responsible for giving the final categorization. The mistake expected to happen during the training of the CNN model is measured using different loss functions in the final layer. This inaccuracy reveals the disparity in both the observed and forecast production. The CNN's estimated output (also called prediction) is the main thing to consider. The label is the second thing that is shown as a result. Different ways to measure how much something is lost are used for different problems. More information regarding different types of loss functions can be found in [65, 66].

In CNNs, Mean Absolute Error (MAE) or Mean Squared Error (MSE) are usually used to deal with regression problems. MAE calculates the mean of the absolute error between the predicted and actual values, while MSE calculates the mean of the square error between the foregoing values. MAE is more robust to outliers than MSE because MSE calculates the square error of outliers. However, the result of MSE is derivable to control the update rate. On the other hand, the result of MAE is nonderivable, the update speed of which cannot be determined during optimization. Therefore, if there are many outliers in the training set and they may negatively impact models, MAE is better than MSE. Otherwise, MSE should be considered. MAE and MSE can be calculated using Equations 6-7.

$$MAE = \frac{\sum_{i=1}^n |y_i - \hat{y}_i|}{n} \quad (6)$$

$$MSE = \frac{\sum_{i=1}^n (y_i - \hat{y}_i)^2}{n} \quad (7)$$

where  $y_i$  is the prediction,  $\hat{y}_i$  is true value and  $n$  is the number of samples.

### 3. Case study

The Zenouz Kaolin Mine, located in part of the Tertiary volcanic province Northwestern Iran, is famous for its high-quality kaolinite deposits. This section provides a detailed geological characterization of the Zenouz deposit, emphasizing its importance for accurate modeling and description in mining operations.

Petrological studies reveal that the study area is mainly composed of two types of rocks: andesite and dacite. These rocks are highly fractured and tectonized, and due to a high degree of alteration in some parts, valuable kaolinite deposits have formed. The pyroclastic rocks present in the area are in the form of volcanic breccia, which contains angular fragments of andesite and dacite along with tuff, and layering is also observed in them. Petrological studies carried out in the study area show that volcanic activity in the region began with the extrusion of pyroclastic rocks in an explosive manner, which gradually gave way to effusive eruptions, resulting in the formation of lava flows and volcanic domes. Based on the geology of the region and laboratory studies, it can be stated that a period of hydrothermal activity occurred as the last stage of volcanic activity in the region, which continued in the form of hot spring activity. Therefore, considering this issue and the thickness and quality of the kaolinites of the region, it is highly probable that Zenouz kaolin has a hydrothermal origin, in which the infiltration of hot solutions caused the decomposition and disintegration of the structural network of aluminum silicates, especially alkaline feldspars. The deposit is structurally controlled by a series of fractures and faults that facilitated the hydrothermal alteration of the host volcanic rocks. These structural features are crucial for

understanding the distribution and quality of the kaolinite.

**4. Methodology**

This study was conducted at the Zenouz kaolin mine near Zenouz city in East Azerbaijan, Iran. The obtained cores samples and information during the exploration stage were then utilized to design the mine, estimate the ore reserves, and undertake the mine planning.

Figure 7 shows two methods of operational flowcharts. According to this figure, a boring machine prepares the drilled cores before the procedure begins. Drilled cores are given to the logging department after the process, which is followed by a logging operation. At this stage, specialists examine the boxes of drilled cores and divide them into two similar sides to prepare

photos and samples. This is the point at which the process is split into two distinct operations. The first is the traditional approach, which entails sending samples to the lab for chemical and physical tests that are uniquely identified by specific codes. This method is more expensive due to chemical reagents, oven energy consumption, and personal expenditures compared to the AI technique, which uses the sample photos as input for a CNN-based machine for kaolinite-type identification. Additionally, another method just requires a few minutes to identify the different forms of kaolinite, whereas the standard method requires processing analyses over a few days to determine the mineral type. It is evident by comparing the accuracy rates of the two approaches that both have trustworthy and respectable rates.

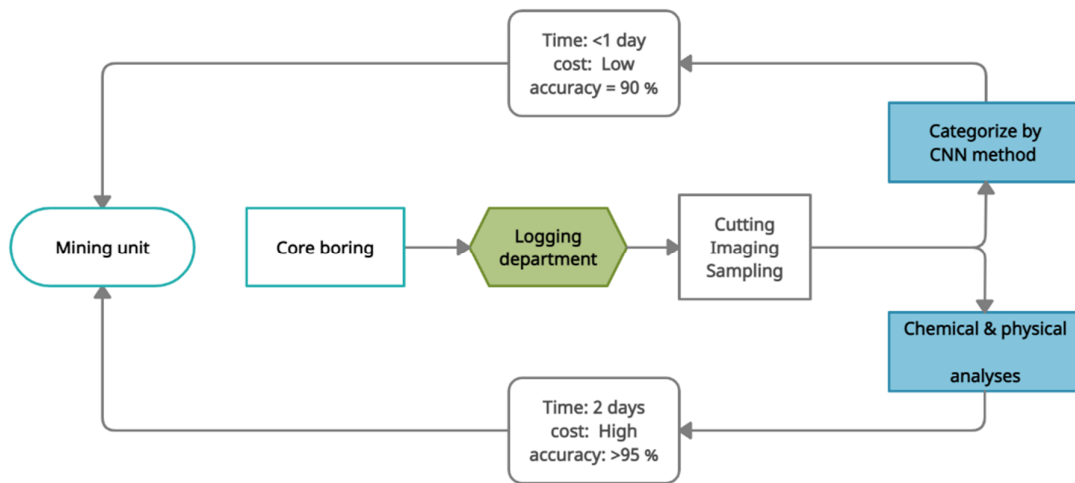


**Figure 7. Summary of two operational ways**

**4.1. Sample preparation**

Figure 8 shows an example of a drilled core's stocking box containing information from a borehole. Since kaolinite is categorized into different types, drilled cores should be taken at specific intervals. This interval is considered two meters on a technical and economic basis.

In the logging section, drilled cores are pre-logged, and two-meter intervals are separated

based on core characteristics to complete this stage. Then, as shown in Figure 9, the cores are cut into two fully similar parts. At this stage of the process, the first half of the cores are archived in the boxes for further analysis, and the second half is labeled with a unique code and delivered to the laboratory for chemical and physical analysis and kaolinite-type determination.



Figure 8. Drilled core's stocking box

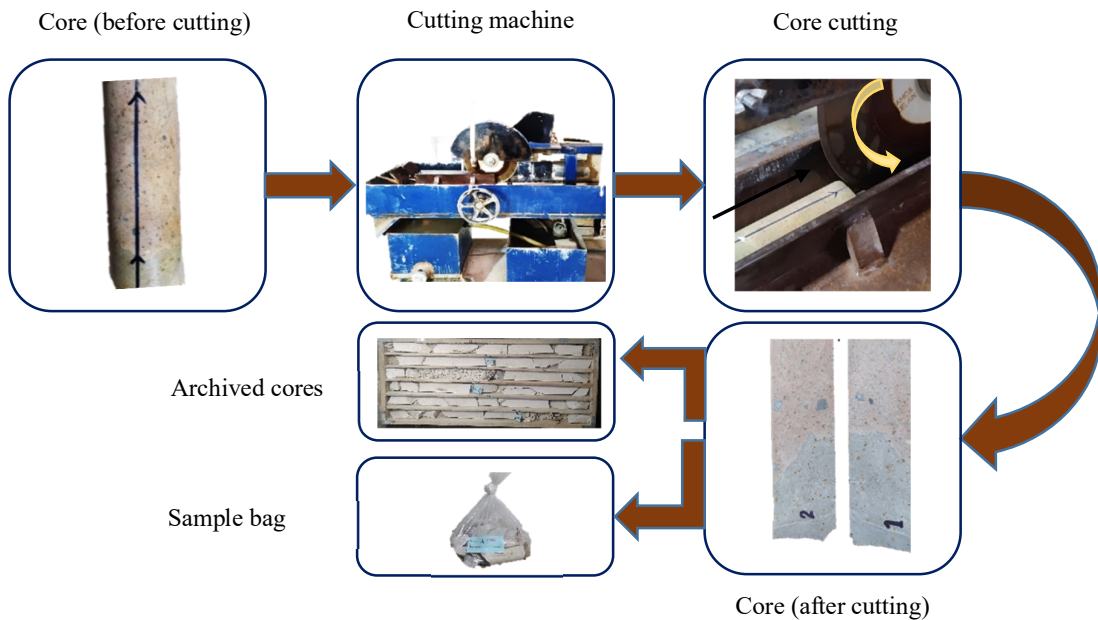


Figure 9. Process of sample preparation

Typically, kaolinite is divided into groups based on chemical and physical analyses. Some of these characteristics are known as disturbing values, in which an increase of these values, like iron oxide ( $Fe_2O_3$ ) and oxides of calcium ( $CaO$ ), plummets the quality and causes kaolinite to have less value. Nevertheless, variables like the oxide of aluminum

( $Al_2O_3$ ), whiteness, and modulus of rupture (M.O.R.) play a crucial role in the determination process and enhance the quality of kaolinite. Table 1 shows how the samples from the Zenouz kaolin mine are divided into six subgroups based on physical and chemical characteristics.

**Table 1. Characteristics of different kaolinite types based on physical and chemical properties**

Type	Al <sub>2</sub> O <sub>3</sub> (%)	Fe <sub>2</sub> O <sub>3</sub> (%)	CaO (%)	Whiteness (%)	M.O.R (Kg/cm <sup>2</sup> )
1	17-20	1-4	3-6	0.0-50	10-20
2	15-17	0.2-0.4	0-0.5	60-100	7-17
3	15-18	0.2-0.5	2-2.5	0-50	0-10
4	15-20	0.2-1.5	2-3	60-75	0-5
5	14-18	0.4-0.8	3-5	70-90	5-15
6	14-18	0.5-1.2	4-6	50-80	5-20

**4.2. Images acquisition**

More than 1000 images of cut drilled cores were captured in similar conditions with a vertical angle and steady light from a 10 cm height to generate an appropriate database for model training. All images were examined, and 610 high-quality images with a resolution of 666×500 pixels were selected for further processing.

**4.3. Chemical and physical tests**

Minerals like kaolinite are classified based on the number of impurities, unwanted components, and physical characteristics. Therefore, kaolinite samples were categorized in Table 2 based on five critical properties, including the percentage of

Fe<sub>2</sub>O<sub>3</sub>, Al<sub>2</sub>O<sub>3</sub>, and CaO as chemical variables and the percentage of whiteness and the module of ruptures (Kg/cm<sup>2</sup>) as physical factors. Table 2 shows examples of the results of analyses for different samples.

**4.4. Assumptions**

In this research, it is assumed that each image shares the same characteristics as the other parts of the sample; therefore, the content of the images is extrapolated to all sections at two-meter intervals. In other words, if drilled cores are cut at any angle and depth, all slices will have the same features. Figure 10 shows 2D samples (images) that also reveal properties of the entire interval.

**Table 2. Example of kaolinite type categorization**

Sample No.	Al <sub>2</sub> O <sub>3</sub> (%)	Fe <sub>2</sub> O <sub>3</sub> (%)	CaO (%)	Whiteness (%)	M.O.R (Kg/cm <sup>2</sup> )	Type
A01563	18.21	3.3	3.68	47.6	17.3	1
A01564	16.66	0.39	2.25	71.1	4.52	4
A01565	17.55	1.18	4.31	44.9	15.11	1
A01566	17.63	1.12	4.4	47.3	16.9	1
A01567	15.55	0.36	2.66	44.6	7.36	3

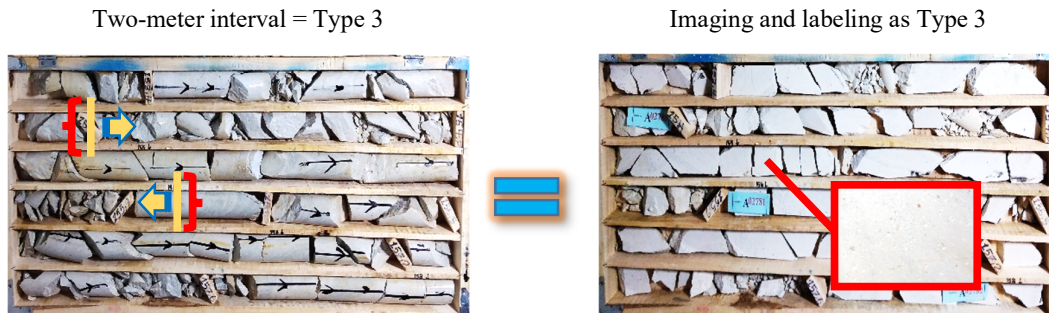


**Figure 10. Example of image sample assumptions**

**4.5. Data collection**

Drilled cores that had previously been analyzed and classified based on chemical and physical

analyses were used to create and build a reliable and valid labeled dataset. Then, images of these cores were taken in equal circumstances, with the

same brightness and distance between the camera and the samples. For each of the six kaolinite types, images with a resolution of 666×500 pixels were chosen (see Figure 11).

Sixty percent of the images were used for training the CNN models, and the rest were used for the validating stage. Table 3 indicates the number and categories of images taken for each kaolinite type. Figure 12 shows some instances of various image categories.

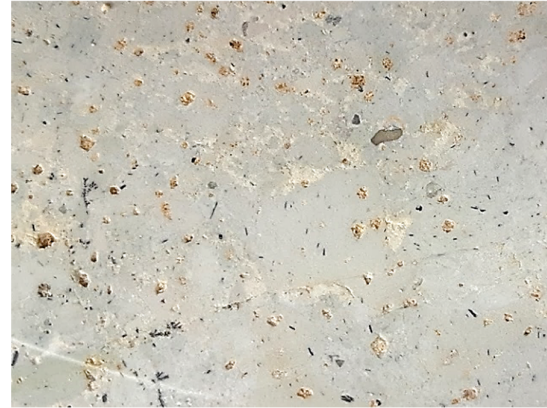


Figure 11. Taken image of kaolinite sample

Table 3. Number of images dedicated to training and validation stages

Kaolinite types	Number of images	Selected images	
		Training	Validation
Type 1	100	60	40
Type 2	120	72	48
Type 3	80	48	32
Type 4	80	48	32
Type 5	120	72	48
Type 6	110	66	44

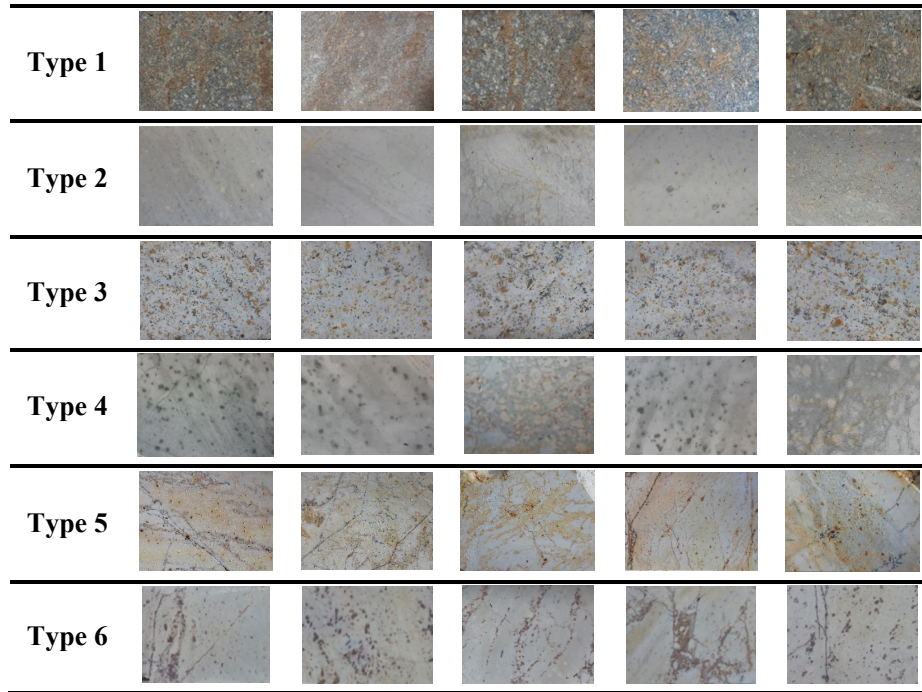


Figure 12. Images of kaolinite samples for each category

#### 4.6. Dataset preprocessing

If the objective is to extend the sum of accessible information and maintain a strategic distance from the overfitting issue, data

augmentation techniques are one possible solution [67-69]. These methods are data-space arrangements for any limited-data issue. Data augmentation consolidates a collection of strategies that progress the properties and estimate

of preparing datasets. Hence, DL systems can perform better when these methods are employed.

On the other hand, a re-scaling method was employed in which the original images include RGB variables in the band of 0-255, but such values are too large for models to comprehend; therefore, re-scaling converts selected values between 0 and 1 rather than the previously indicated range by downsizing through the use of a 1/255 ratio.

The acquisition of sufficient training samples forms a pivotal aspect in training DNN. However, obtaining drill core image data in the context of

underground engineering poses a notable challenge. Data augmentation involves generating additional data by executing a set of stochastic modifications on the training dataset, which amplifies the amount and diversity of data and diminishes the network's reliance on certain image features. This study examines a variety of image processing techniques, including upside-down or left-right turnover, random cropping, and color change. The online data augmentation method was integrated with various techniques, as exhibited in Figure 13.

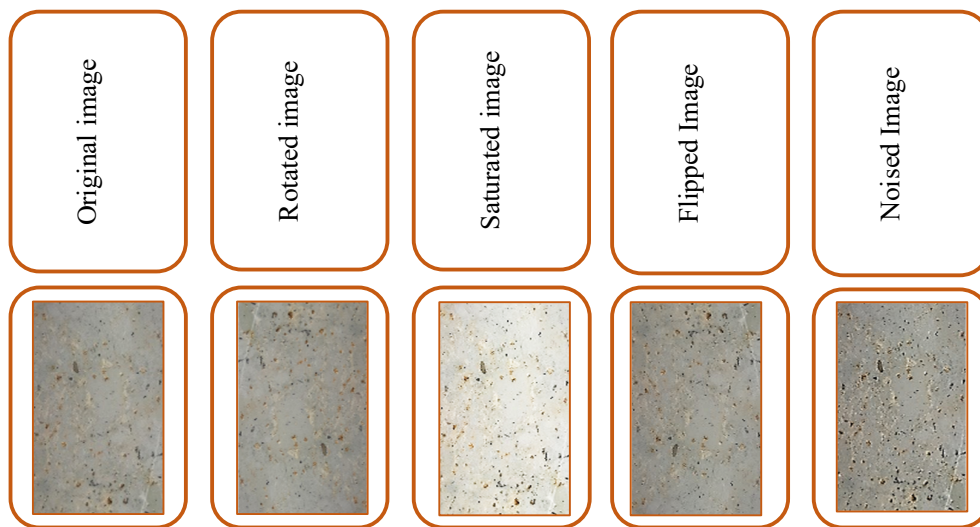


**Figure 13. Five used data augmentation techniques**

## 5. Model generation

The input images were reduced from 666×500 pixels to 100×100 pixels to create a CNN topology and recognize the type of kaolinite samples. This helps to understand the model better and decreases computing volume. Convolutional layers are typically limited to 5 layers; however, extra layers were designed in this study to maximize the classification accuracy of the samples by

considering the sample's significant and complicated details and the necessity for high precision as two essential factors. The parameters of all different CNN structures are shown in Table 4.

The accuracy and the loss of eight different topologies were evaluated to determine the sample types based on input data. Figures 14 and 15 illustrate the accuracy and loss of different considered structures, respectively.

**Table 4. CNNs' different structures**

Structure name	No. of layers	Architecture
Structure A	8	Conv2D (32*3*3),Maxpooling 2D (2*2), Conv2D (32*3*3), maxpooling 2D (2*2), Flatten layer (40000), Dense layer (64), Drop out (0.5), FC Dense layer (6) <b>Total params = 2569606</b>
Structure B	8	Conv2D (64*3*3),Maxpooling 2D (2*2), Conv2D (64*3*3), maxpooling 2D (2*2), Flatten layer (40000), Dense layer (64), Drop out (0.5), FC Dense layer (6) <b>Total params = 3789258</b>
Structure C	6	Conv2D (32*3*3),Maxpooling 2D (2*2), Flatten layer (40000), Dense layer (64), Drop out (0.5), FC Dense layer (6) <b>Total params = 789696</b>
Structure D	6	Conv2D (16*3*3),Maxpooling 2D (2*2), Flatten layer (40000), Dense layer (64), Drop out (0.5), FC Dense layer (6) <b>Total params = 352146</b>
Structure E	10	Conv2D (64*3*3),Maxpooling 2D (2*2), Conv2D (64*3*3),Maxpooling 2D (2*2), Conv2D (64*3*3), maxpooling 2D (2*2), Flatten layer (40000), Dense layer (64), Drop out (0.5), FC Dense layer (6) <b>Total params = 5682274</b>
Structure F	6	Conv2D (16*3*3),Maxpooling 2D (2*2), Flatten layer (40000), Dense layer (64), Drop out (0.5), FC Dense layer (6) <b>Total params = 363528</b>
Structure G	8	Conv2D (128*3*3),Maxpooling 2D (2*2), Conv2D (128*3*3), maxpooling 2D (2*2), Flatten layer (40000), Dense layer (64), Drop out (0.5), FC Dense layer (6) <b>Total params = 6875464</b>
Structure H	8	Conv2D (16*32*3),Maxpooling 2D (2*2), Conv2D (16*32*3), maxpooling 2D (2*2), Flatten layer (40000), Dense layer (64), Drop out (0.5), FC Dense layer (6) <b>Total params = 642758</b>

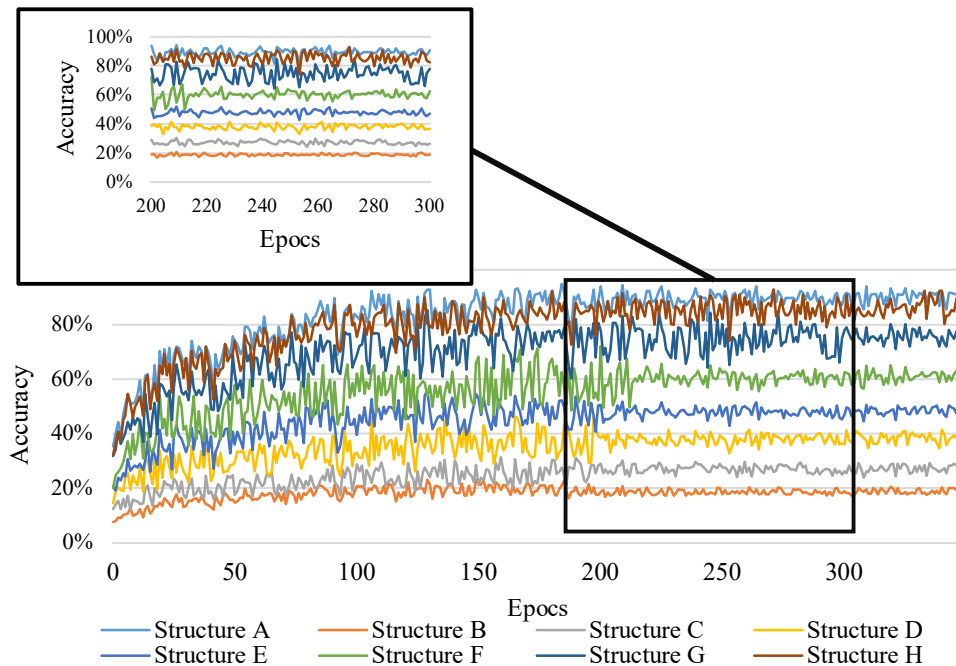


**Figure 14. Accuracy of eight different CNN structures**

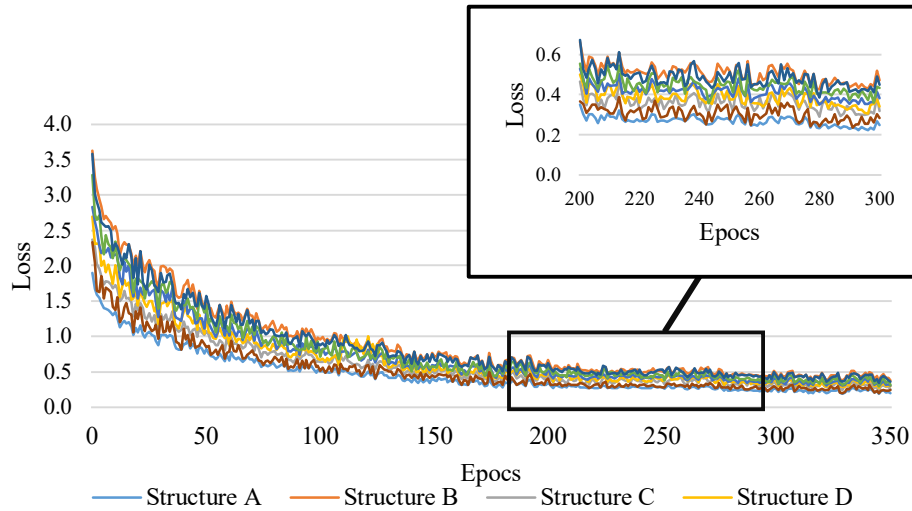


**Figure 15. Loss of eight different CNN structures**

Figures 14 and 15 show that the best structure to determine the sample types are structures A and H. Figure 16 shows the structure of these eight-layer CNN models developed in this study. In this structure, images are input to the model in  $100 \times 100 \times 3$  shapes, meaning the images are  $100 \times 100$  pixels in size and contain three colors (Red, Green, and Blue). The first layer is an  $(X) \times 3 \times 3$  shape 2D convolutional layer that the first argument controls the number of output channels for the layer (e.g., 16 or 32). In this layer, the same padding is used to ensure the output shape is the same as the input. After the convolutional layer, a

max-pooling layer calculates the maximum value for feature map patches. The structure utilizes it to produce a sub-sampled new feature with a pool size of  $2 \times 2$ . Both mentioned layers (convolutional and pooling) are repeated, and in the next phase, the flattened layer is designed to convert 2D feature maps to 1D. The first dense layer is built to create 64 fully connected neurons. Then, the drop-out layer of 50% is used to reduce overfitting in the network. Finally, the last layer is a dense layer with six neurons that recognize six different types of kaolinite samples.

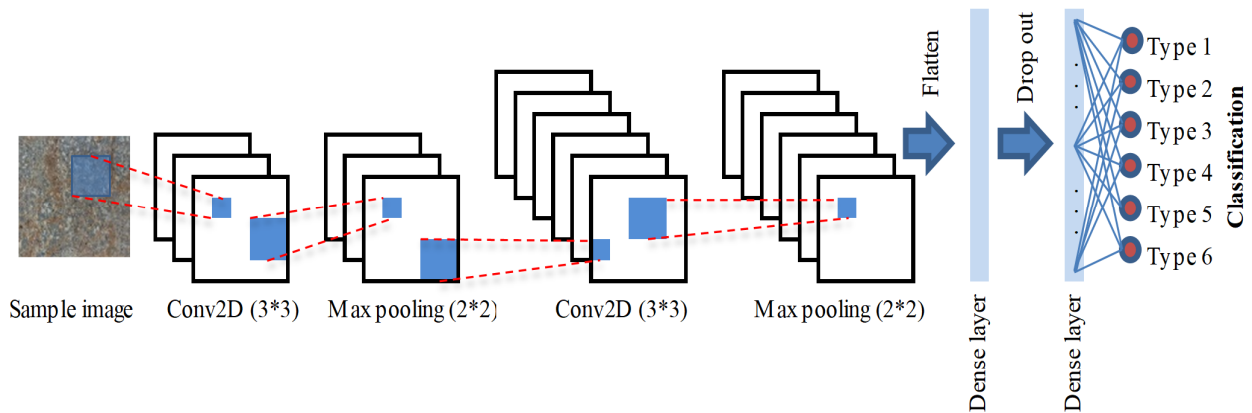


**Figure 16. Structure of the developed eight-layer CNN model in this study**

Eventually, the model detected sample types based on their related folders and performed training and validation data with 300 steps per batch size. Due to the accuracy, which had achieved a fixed state after 300 epochs, the model

was completed in 300 epochs to avoid wasting time and expanding the volume of calculations.

### 6. Model validation

Following a comparison of structures A and H, model A was identified as the most efficient model for training and recognizing sample types, with 90% accuracy versus 84% for model H. Figure 17

compares the accuracy and loss trends of the two models through 300 epochs.

Other unique methods described below were employed to validate and measure the selected model's efficiency.

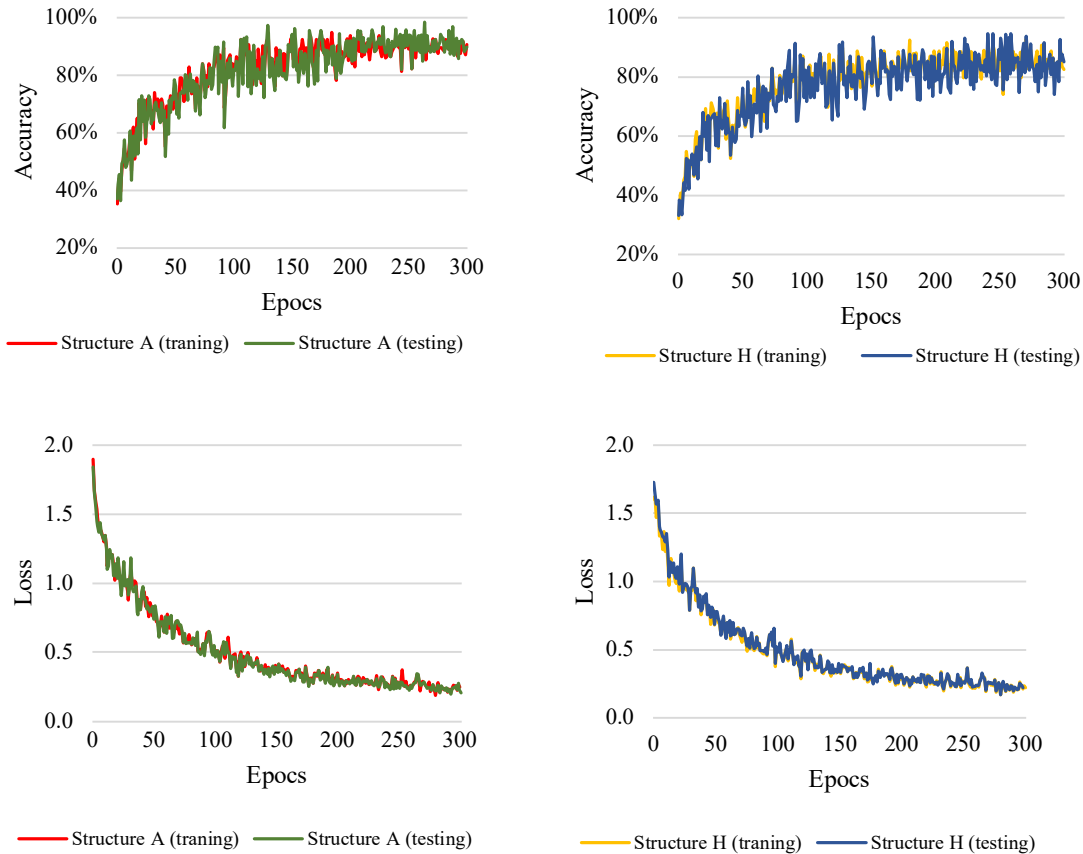


Figure 2. Accuracy and loss of structures A and H

#### 6.1. Accuracy

The accuracy metric is technically expressed as the ratio of accurate classification generated by the model and is formally defined as [70]:

$$Accuracy = \frac{\text{Number of correct predictions}}{\text{Total number of predictions}} \quad (8)$$

This method was used to assess the accuracy of the A and H models for each category of kaolinite types, as shown in Figure 18.

According to Figure 18, model A is more accurate than model H. Therefore, three additional methods, including precision, recall, and F1-score,

were used to better illustrate the efficiency of model A.

#### 6.2. Precision

The precision for a category in a classification model is the number of true positives divided by the total number of elements labeled as a positive class (Equation 9) [70, 71].

$$Precision = \frac{\text{True positive}}{\text{True positive} + \text{False positive}} \quad (9)$$

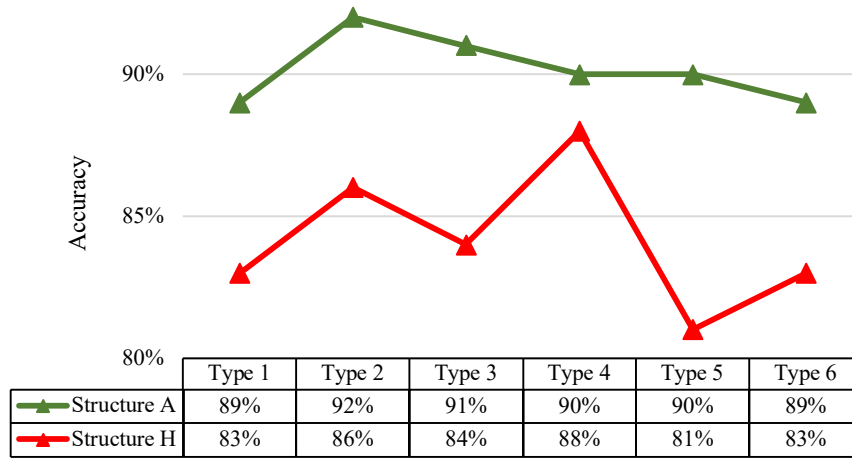


Figure 18. Accuracy of models A and H for identifying kaolinite types

6.3. Recall:

Recall is defined as the number of true positives divided by the total number of components that actually belong to the positive class (Equation 10) [71, 72].

$$Recall = \frac{True\ positive}{True\ positive + False\ negative} \quad (10)$$

6.4. F1-score

The F1-score, the harmonic mean of precision and recall, measures a test's accuracy. The F1-score metric can also have a maximum value of 1.0, indicating perfect precision and recall, and a minimum value of 0 if neither precision nor recall is zero [72, 73].

$$F1 - score = 2 * \frac{Recall * Precision}{Recall + Precision} \quad (11)$$

All four performance indices mentioned above were calculated in this paper to comprehend the model's reliability better. Figure 19 summarizes the results for different types of kaolinite. From the figure, it could be comprehended that, however, precision and recall values are perfect for types 4 and 1, respectively, and type 2 is the best-fit dataset due to the performance of the model. Furthermore, type 6, except for precision, has the lowest value of the rest of the methods. Besides, types 3 and 5 had exactly the same performance in all four methods.

6.5. Geological and mineralogical validation

To strengthen the validation process of our machine vision algorithm for ore-type detection in drilling cores, we conducted a thorough analysis that extends to cross-referencing with geological maps of the mine and district [74], [75]. This comprehensive approach not only enhances the robustness of our validation but also establishes a strong correlation between machine-generated results and geological realities.

The spatial distribution of predicted ore types aligns remarkably well with known geological formations and mineralization zones delineated on the maps. This alignment serves as a pivotal validation step, bolstering our confidence in the algorithm's efficacy in interpreting drilling cores within their geological contexts. In our validation efforts, we consider the elemental compositions identified within the drilling cores and their complementary color variations. Through collaboration with experts in mineralogy and geology, we determine patterns linking specific elements to distinct color manifestations within the samples. By combining this knowledge into our algorithm, we enable it to not only detect the presence of these elements but also infer potential ore types based on observed color variations. Additionally, expert geologists and mineralogists provide invaluable insights, validating the algorithm's interpretations based on their extensive knowledge of geological formations and

mineralization patterns. By integrating these validation methods, including cross-referencing with geological maps, field observations, and expert review, we not only validate the algorithm's performance but also establish a strong foundation for its practical application in ore type detection. This holistic approach ensures that our machine vision algorithm remains firmly grounded in geological and mineralization evidence, investing confidence in its reliability and accuracy.

In future studies, we aim to further expand the capabilities of our research by delving into the

domain of deep learning algorithms to demonstrate mineral percentages within drilling cores. This endeavor represents a natural progression from our current focus on ore-type detection, allowing us to delve deeper into the quantitative aspects of mineral composition. By leveraging advanced deep learning techniques, we expect to develop algorithms capable of not only identifying minerals but also estimating their relative abundance within the cores.

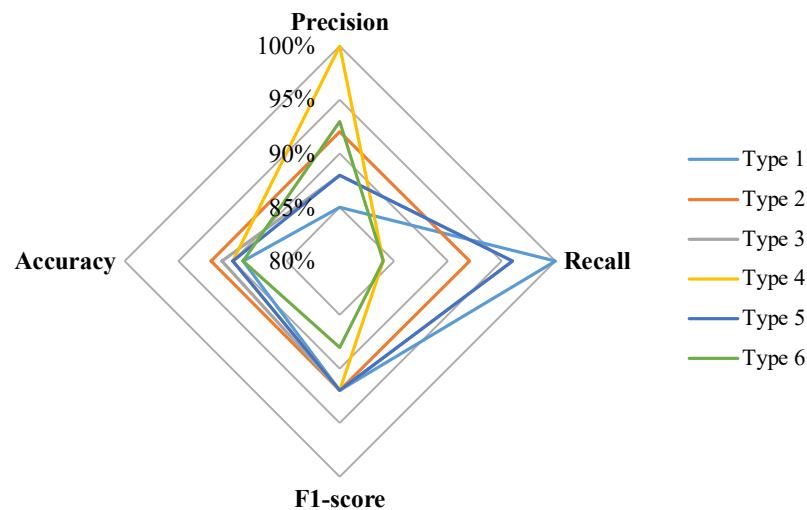


Figure 19. Four distinct methods to evaluate model A's efficiency

## 7. Conclusions

DL has made considerable advances in a spectrum of uses in current history. DL automatically detects characteristics and patterns from inputs mixed with modeling frameworks capable of capturing highly complex behavior, unlike conventional ML approaches. With high accuracy and ability to cope with image data, CNNs are the most widely available platform which has been used extensively in various fields.

Since classifying the types of ore types in drilled cores using conventional laboratory-based techniques is a costly and time-consuming procedure, a novel DL-based model was developed in this study to overcome this challenge. Eight different CNN models (A to H) were tested on six distinct kaolinite types compiled from a kaolinite mine in Iran, which were categorized in the

laboratory based on their chemical and physical characteristics. After validation of all models by evaluating their accuracy and loss parameters, two eight-layer models including A and H were chosen as accurate models due to their more accuracy in comparison to other six models. According to a comparison between the two models, model A, with 90% accuracy, outperformed model H, with 84%, in learning from previously analyzed and categorized drilled cores' photos. Finally, the robustness of model A in kaolinite types identifying was further evaluated using three criteria, including precision, recall, and F1-score. The values of 92%, 92%, and 90%, were respectively obtained for the foregoing indices, representing the high performance of the developed model in kaolinite type detection.

## Funding

This research received no external funding.

## Conflicts of Interest

The authors declare no conflicts of interest.

## References

- [1]. Dominy, S. C., Platten, I. M., Xie, Y., & Minnitt, R. C. A. (2010). Underground grade control protocol design: Case study from the Liphichi gold project, Larecaja, Bolivia. *Applied Earth Science*, 119(4), 205–219.
- [2]. Stanley, C. R., & Smee, B. W. (2007). Strategies for reducing sampling errors in exploration and resource definition drilling programmes for gold deposits. *Geochemistry: Exploration, Environment, Analysis*, 7(4), 329–340.
- [3]. Pitard, F. F., & Pitard, F. F. (2019). *Theory of sampling and sampling practice* (3rd ed.). Taylor & Francis.
- [4]. Lepistö, L. (2005). Rock image classification using color features in Gabor space. *Journal of Electronic Imaging*, 14(4), 040503.
- [5]. Singh, V., & Mohan Rao, S. (2005). Application of image processing and radial basis neural network techniques for ore sorting and ore classification. *Minerals Engineering*, 18(15), 1412–1420.
- [6]. Baykan, N. A., & Yilmaz, N. (2010). Mineral identification using color spaces and artificial neural networks. *Computers & Geosciences*, 36(1), 91–97.
- [7]. Khorram, F., Memarian, H., & Tokhmechi, B. (2012). Limestone chemical components estimation using image processing and pattern recognition techniques. *International Journal of Mining Science and Technology*, 2(2), 126–135.
- [8]. Keyvani, A., & Strom, K. (2013). A fully-automated image processing technique to improve measurement of suspended particles and flocs by removing out-of-focus objects. *Computers & Geosciences*, 52, 189–198.
- [9]. Liu, C., Tang, C. S., Shi, B., & Bin Suo, W. (2013). Automatic quantification of crack patterns by image processing. *Computers & Geosciences*, 57, 77–80.
- [10]. Gan, S. Q., & Scholz, C. A. (2013). Extracting paleoclimate signals from sediment laminae: An automated 2-D image processing method. *Computers & Geosciences*, 52, 345–3.
- [11]. Patel, A. K., & Chatterjee, S. (2016). Computer vision-based limestone rock-type classification using probabilistic neural network. *Geoscience Frontiers*, 7(1), 53–60.
- [12]. Chauhan, S., Kumar, P., Gupta, A., & Kumar, P. (2016). Processing of rock core microtomography images: Using seven different machine learning algorithms. *Computers & Geosciences*, 86, 120–128.
- [13]. Maiti, A., Chakravarty, D., Biswas, K., & Halder, A. (2017). Development of a mass model in estimating weight-wise particle size distribution using digital image processing. *International Journal of Mining Science and Technology*, 27(3), 435–443.
- [14]. Ramil, A., López, A. J., Pozo-Antonio, J. S., & Rivas, T. (2018). A computer vision system for identification of granite-forming minerals based on RGB data and artificial neural networks. *Measurement*, 117, 90–95.
- [15]. Maitre, J., Bouchard, K., & Bédard, L. P. (2019). Mineral grains recognition using computer vision and machine learning. *Computers & Geosciences*, 130(February), 84–93.
- [16]. Ran, X., Xue, L., Zhang, Y., Liu, Z., Sang, X., & He, J. (2019). Rock classification from field image patches analyzed using a deep convolutional neural network. *Unpublished manuscript*, 1–16.
- [17]. Ouanan, H., & Abdelwahed, E. H. (2019). Image processing and machine learning applications in the mining industry: Mine 4.0. In *Proceedings of the 2019 International Conference on Intelligent Systems and Advanced Computing (ISACS 2019)* (pp. 1–5). IEEE.
- [18]. Safari, H., Balcom, B. J., & Afrough, A. (2021). Characterization of pore and grain size distributions in porous geological samples – An image processing workflow. *Computers & Geosciences*, 156(June), 104895.
- [19]. Liu, Y., Zhang, Z., Liu, X., Wang, L., & Xia, X. (2021). Deep learning-based image classification for online multi-coal and multi-class sorting. *Computers & Geosciences*, 157(August), 104922.
- [20]. Fathi, M., Alimoradi, A., & Ahooi, H. H. (2021). Optimizing Extreme Learning Machine Algorithm using Particle Swarm Optimization to estimate iron ore grade. *Journal of Mining and Environment*, 12(2), 397–411.
- [21]. Alimoradi, A., Maleki, B., Karimi, A., Sahafzadeh, M., & Abbasi, S. (2020). Integrating geophysical attributes with new cuckoo search machine-learning algorithm to estimate silver grade values: Case study at Zarshouran Gold Mine. *Journal of Mining and Environment*, 11(3), 865–879.
- [22]. Farhadi, S., Tatullo, S., Boveiri Konari, M., & Afzal, P. (2024). Evaluating StackingC and ensemble models for enhanced lithological classification in geological mapping. *Journal of Geochemical Exploration*, 260(February), 107441.
- [23]. Farhadi, S., Afzal, P., Konari, M. B., Saein, L. D., & Sadeghi, B. (2022). Combination of machine learning algorithms with concentration–area fractal method for soil geochemical anomaly detection in sediment–hosted Irankuh Pb–Zn deposit, Central Iran. *Minerals*, 12(6).

- [24]. Afzal, P., Farhadi, S., Konari, M. B., Meigoony, M. S., & Saein, L. D. (2022). Geochemical anomaly detection in the Irankuh District using hybrid machine learning technique and fractal modeling. *Geopersia*, 12(1), 191–199.
- [25]. Géron, A. (2017). *Hands-on machine learning with Scikit-Learn and TensorFlow*. O'Reilly Media, Inc.
- [26]. Fu, Y., & Aldrich, C. (2020). Deep learning in mining and mineral processing operations: A review. *IFAC-PapersOnLine*, 53(2), 11920–11925.
- [27]. Alzubaidi, L., et al. (2021). Review of deep learning: Concepts, CNN architectures, challenges, applications, future directions. *Journal of Cloud Computing: Advances, Systems and Applications*, 8(1).
- [28]. Socher, R., et al. (2013). Recursive deep models for semantic compositionality over a sentiment treebank. In *Proceedings of the 2013 Conference on Empirical Methods in Natural Language Processing (EMNLP)*.
- [29]. Fang, W., Love, P. E. D., Luo, H., & Ding, L. (2020). Computer vision for behaviour-based safety in construction: A review and future directions. *Advanced Engineering Informatics*, 43(February), 100980.
- [30]. Palaz, D., Magimai-Doss, M., & Collobert, R. (2019). End-to-end acoustic modeling using convolutional neural networks for HMM-based automatic speech recognition. *Speech Communication*, 108, 15–32.
- [31]. Li, H. C., Deng, Z. Y., & Chiang, H. H. (2020). Lightweight and resource-constrained learning network for face recognition with performance optimization. *Sensors (Switzerland)*, 20(21), 1–20.
- [32]. Caggiano, A., Zhang, J., Alfieri, V., Caiazzo, F., Gao, R., & Teti, R. (2019). Machine learning-based image processing for on-line defect recognition in additive manufacturing. *CIRP Annals*, 68(1), 451–454.
- [33]. Zhang, B., Jaiswal, P., Rai, R., Guerrier, P., & Baggs, G. (2019). Convolutional neural network-based inspection of metal additive manufacturing parts. *Rapid Prototyping Journal*, 25(3), 530–540.
- [34]. Liu, Y., Guo, L., Gao, H., You, Z., Ye, Y., & Zhang, B. (2022). Machine vision based condition monitoring and fault diagnosis of machine tools using information from machined surface texture: A review. *Mechanical Systems and Signal Processing*, 164, 108068.
- [35]. Bhowmick, S., Nagarajaiah, S., & Veeraraghavan, A. (2020). Vision and deep learning-based algorithms to detect and quantify cracks on concrete surfaces from UAV videos. *Sensors*, 20(21), 6299.
- [36]. Fang, W., Love, P. E. D., Luo, H., & Ding, L. (2020). Computer vision for behaviour-based safety in construction: A review and future directions. *Advances in Engineering Informatics*, 43, 100980.
- [37]. Cireşan, D., Meier, U., Masci, J., & Schmidhuber, J. (2012). Multi-column deep neural network for traffic sign classification. *Neural Networks*, 32, 333–338.
- [38]. Li, Y., Zhang, T., Sun, S., & Gao, X. (2019). Accelerating flash calculation through deep learning methods. *Journal of Computational Physics*, 394, 153–165.
- [39]. Han, W., Feng, R., Wang, L., & Gao, L. (2018). Adaptive spatial-scale-aware deep convolutional neural network for high-resolution remote sensing imagery scene classification. In *IGARSS 2018 - 2018 IEEE International Geoscience and Remote Sensing Symposium* (pp. 4736–4739). IEEE.
- [40]. Chen, H., Engkvist, O., Wang, Y., Olivecrona, M., & Blaschke, T. (2018). The rise of deep learning in drug discovery. *Drug Discovery Today*, 23(6), 1241–1250.
- [41]. Benhammou, Y., Achchab, B., Herrera, F., & Tabik, S. (2020). BreakHis based breast cancer automatic diagnosis using deep learning: Taxonomy, survey and insights. *Neurocomputing*, 375, 9–24.
- [42]. Wulczyn, E., et al. (2020). Deep learning-based survival prediction for multiple cancer types using histopathology images. *PLoS ONE*, 15(6), e0233678.
- [43]. Esteva, A., et al. (2017). Dermatologist-level classification of skin cancer with deep neural networks. *Nature*, 542(7639), 115–118.
- [44]. Jamshidi, M., et al. (2020). Artificial intelligence and COVID-19: Deep learning approaches for diagnosis and treatment. *IEEE Access*, 8, 109581–109595.
- [45]. De Fauw, J., et al. (2018). Clinically applicable deep learning for diagnosis and referral in retinal disease. *Nature Medicine*, 24(9), 1342–1350.
- [46]. Mohanty, S. P., Hughes, D. P., & Salathé, M. (2016). Using deep learning for image-based plant disease detection. *Frontiers in Plant Science*, 7.
- [47]. Sladojevic, S., Arsenovic, M., Anderla, A., Culibrk, D., & Stefanovic, D. (2016). Deep neural networks based recognition of plant diseases by leaf image classification. *Computational Intelligence and Neuroscience*, 2016, 1–11.
- [48]. Chen, Y., Lin, Z., Zhao, X., Wang, G., & Gu, Y. (2014). Deep learning-based classification of hyperspectral data. *IEEE Journal of Selected Topics in Applied Earth Observations and Remote Sensing*, 7(6), 2094–2107.
- [49]. Lee, S. H., Chan, C. S., Wilkin, P., & Remagnino, P. (2015). Deep-plant: Plant identification with convolutional neural networks. In *2015 IEEE International Conference on Image Processing (ICIP)* (pp. 452–456). IEEE.
- [50]. Bhattacharya, S., Tripathi, S. L., & Kamboj, V. K. (2023). Design of tunnel FET architectures for low power application using improved Chimp optimizer

- algorithm. *Engineering Computations*, 39(2), 1415–1458.
- [51]. Bruno, D. R., & Osorio, F. S. (2017). Image classification system based on deep learning applied to the recognition of traffic signs for intelligent robotic vehicle navigation purposes. In *2017 Latin American Robotics Symposium (LARS) and 2017 Brazilian Symposium on Robotics (SBR)* (pp. 1–6). IEEE.
- [52]. Madan, R., Agrawal, D., Kowshik, S., Maheshwari, H., Agarwal, S., & Chakravarty, D. (2019). Traffic sign classification using hybrid HOG-SURF features and convolutional neural networks. In *Proceedings of the 8th International Conference on Pattern Recognition Applications and Methods* (pp. 613–620). SCITEPRESS - Science and Technology Publications.
- [53]. He, Y., Zhang, L., Chen, Z., & Li, C. Y. (2022). A framework of structural damage detection for civil structures using a combined multi-scale convolutional neural network and echo state network. *Engineering Computations*
- [54]. Alzubaidi, L., et al. (2021). Review of deep learning: Concepts, CNN architectures, challenges, applications, future directions. *Journal of Big Data*, 8(1). Springer International Publishing.
- [55]. Rawat, W., & Wang, Z. (2017). Deep convolutional neural networks for image classification: A comprehensive review. *Neural Computation*, 29(9), 2352–2449.
- [56]. Valizadeh, M., & Wolff, S. J. (2022). Convolutional neural network applications in additive manufacturing: A review. *Advances in Industrial Engineering*, 4, 100072.
- [57]. Liu, S., McGree, J., Ge, Z., & Xie, Y. (2016). Computer vision in big data applications. In *Computational and Statistical Methods for Analysing Big Data with Applications* (pp. 57–85).
- [58]. Gholamalinezhad, H., & Khosravi, H. (2020). Pooling methods in deep neural networks, a review. *arXiv*. Retrieved from <http://arxiv.org/abs/2009.07485>
- [59]. Li, Z., Liu, F., Yang, W., Peng, S., & Zhou, J. (2022). A survey of convolutional neural networks: Analysis, applications, and prospects. *IEEE Transactions on Neural Networks and Learning Systems*, 33(12), 6999–7019.
- [60]. LeCun, Y., Bottou, L., Bengio, Y., & Haffner, P. (1998). Gradient-based learning applied to document recognition. *Proceedings of the IEEE*, 86(11), 2278–2324.
- [61]. Hinton, G. E. (n.d.). Rectified linear units improve restricted Boltzmann machines.
- [62]. Hagan, M. T., & Beale, M. H. (n.d.). *Neural network design*.
- [63]. Shea, K. O., & Nash, R. (2015). An introduction to convolutional neural networks (pp. 1–11).
- [64]. Dumoulin, V., & Visin, F. (2018). A guide to convolution arithmetic for deep learning (pp. 1–31).
- [65]. Wang, Q., Ma, Y., Zhao, K., & Tian, Y. (2022). A comprehensive survey of loss functions in machine learning. *Annals of Data Science*, 9(2), 187–212.
- [66]. Tian, Y., Su, D., Lauria, S., & Liu, X. (2022). Recent advances on loss functions in deep learning for computer vision. *Neurocomputing*, 497, 129–158.
- [67]. Shorten, C., & Khoshgoftaar, T. M. (2019). A survey on image data augmentation for deep learning. *Journal of Big Data*, 6(1), 60.
- [68]. Hirahara, D., Takaya, E., Takahara, T., & Ueda, T. (2020). Effects of data count and image scaling on deep learning training. *PeerJ Computer Science*, 6, e312.
- [69]. Saleh, A. M., & Hamoud, T. (2021). Analysis and best parameters selection for person recognition based on gait model using CNN algorithm and image augmentation. *Journal of Big Data*, 8(1), 1.
- [70]. Metz, C. E. (1978). Basic principles of ROC analysis. *Seminars in Nuclear Medicine*, 8(4), 283–298.
- [71]. Goutte, C., & Gaussier, É. (2005). A probabilistic interpretation of precision, recall and F-score, with implications for evaluation. In *Advances in Information Retrieval* (pp. 345–359).
- [72]. Fränti, P., & Mariescu-Istodor, R. (2023). Soft precision and recall. *Pattern Recognition Letters*, 167, 115–121.
- [73]. Taha, A. A., & Hanbury, A. (2015). Metrics for evaluating 3D medical image segmentation: Analysis, selection, and tool. *BMC Medical Imaging*, 15(1), 29.
- [74]. Mollaei, F. (2014). Identification of promising mineral zones in relation to clay minerals using ETM+ and ASTER data (case study: Marand). In *8th National Specialized Conference of Geology*, Arak.
- [75]. Azad, M. F. (2007). Petrography, geochemistry of major elements and tectonic environment of the benmorite dike in the kaolin mine zone, north of Marand-Azerbaijan. In *7th Conference of the Iranian Economic Geology Society*, Damghan

## شناسایی نوع کانی در مغزه های حفاری با استفاده از الگوریتم بینایی ماشین

پویا نوبهار<sup>۱\*</sup>، یاشار پوررحیمیان<sup>۲</sup>، روح‌الله شیرانی فرادنبه<sup>۳</sup>، و فریدون ملائی کشکی<sup>۴</sup>

۱- مرکز آموزشی ARC، دانشگاه آدلاید، استرالیا

۲- دانشکده معدن و مهندسی نفت، دانشگاه آلبرتا، کانادا

۳- دانشکده معدن، مهندسی مواد معدنی، انرژی و شیمی، دانشگاه کرتین، استرالیا

۴- شرکت صنایع خاک چینی ایران، ایران

ارسال ۲۰۲۴/۰۵/۱۷، پذیرش ۲۰۲۴/۰۸/۳۰

\* نویسنده مسئول مکاتبات: a1900269@adelaide.edu.au

## چکیده:

ارزیابی ذخایر معدنی و شناسایی نوع کانی با استفاده از داده‌های به‌دست‌آمده از چال‌های اکتشافی در طراحی و استخراج معدن اهمیت زیادی دارد. با این حال، آماده‌سازی نمونه‌های مغزه‌های حفاری و انجام آزمایش‌های شیمیایی و فیزیکی فرآیندی زمان‌بر و پرهزینه است که باعث کندی فرآیند مدل‌سازی می‌شود. این مقاله مدلی نوآورانه مبتنی بر یادگیری عمیق برای شناسایی انواع نمونه‌های کاتولینیت ارائه می‌دهد. برای این منظور، از یک مجموعه داده شامل تصاویر مغزه‌های حفاری و انواع آن‌ها که از تحلیل‌های شیمیایی و فیزیکی متداول به‌دست‌آمده بود، استفاده شد. هشت معماری شبکه عصبی کانولوشن (CNN) بر اساس ویژگی‌های منحصر به فرد توسعه داده شد، که به نام‌های A, B, C, D, E, F, G و H نام‌گذاری شدند. شش مورد از این هشت معماری CNN دقتی کمتر از ۸۰ درصد داشتند، در حالی که دو مورد از آن‌ها، مدل‌های A و H، دقت بالاتری نسبت به سایر معماری‌ها داشتند. به دلیل شباهت نتایج، هر دوی آن‌ها به‌طور عمیق‌تر تحلیل شدند. مدل A با دقت ۹۰ درصد، نسبت به مدل B با دقت ۸۴ درصد کارآمدتر بود. علاوه بر این، عملکرد شناسایی کلاس مدل A با استفاده از شاخص‌های مختلفی ارزیابی شد که مقادیر قابل قبولی برای شناسایی نوع نمونه‌ها در شش نوع مختلف کاتولینیت است.

**کلمات کلیدی:** هوش مصنوعی، پردازش تصویر، طبقه‌بندی، بهینه‌سازی، مغزه حفاری، شبکه عصبی کانولوشنی